Computation of the Two-Dimensional Incompressible Turbulent Flow Around a Wing Section in Cascade*

By

Shotaro UTO**

ABSTRACT

Computation of the two-dimensional incompressible turbulent flow around a wind section in cascade was made using the finite difference method.

The computational scheme used in this paper is based on the Implicit Approximate Factorization scheme, which has been developed at the Ship Research Institute.

The overlapping grid technique was used in order to generate well-conditioned, body-fitted coordinates for the complicated computational domain around a cascade wing section easily.

The computed results were compared in two steps. Firstly, the comparative computational study between the present method and the higher-order boundary layer integral method was carried out and the merit and demerit of the present scheme were discussed in detail. Secondly, the comparison with experimental data (lift and drag coefficient) was made. The present method showed reasonable agreement with them.

* Received on May 10, 1989

** Arctic Vessel and Low Temperature Engineering Division

NOMENCLATURE

D	Propeller diameter
H	Propeller pitch
k	Turbulent kinetic energy
l	Chord length of a wing section
p	Static pressure
p_1	Upstream static pressure
R	Propeller radius
R_e	Reynolds number based on upstream uniform velocity and chord length of a wing section
S	Spacing of a wing cascade
U_1, V_1	Upstream uniform velocity components in x and y direction
U_{1n}, V_{1n}	Upstream uniform velocity components in x and y direction (nominal value)
x, y	Cartesian coordinate system with its origin at the leading edge of a wing section
C_p	Pressure coefficient
C_{D1}	Drag coefficient
C_{L1}	Lift coefficient
α_1	Inflow angle
α_{1n}	Inflow angle (nominal value)
α_2	Outflow angle
$\Delta\alpha$	Flow turning angle ($= \alpha_2 - \alpha_1$)
α_m	Geometrical mean flow angle ($= 0.5 \times (\alpha_2 + \alpha_1)$)
β	Coefficient of pseudo-compressibility
γ	Staggered angle of a wing cascade
δ^*	Displacement thickness
θ	Momentum thickness
ν_t	Eddy viscosity
ξ, η	Body-fitted curvilinear coordinate system
σ	Solidity of a wing cascade ($= l/S$)
ω	Coefficient of 4-th order numerical dissipation term

(Notice: Non-dimensionalization is based on the upstream uniform velocity and the chord length of a wing section. The force is decomposed into components parallel and perpendicular to the geometrical mean velocity)

1. INTRODUCTION

The application of the Finite Difference Method (FDM) to the incompressible viscous flow problem has been developed remarkably with the improvement of the computer hardware. In particular, computation of the two-dimensional turbulent flow can be regarded nearly as a practical tool of design and analysis judging from the CPU time and required memory. Nevertheless, we have few quantitative studies on the accuracy of the computed results, especially of the lift and drag coefficients, which are of great importance in engineering problem.

In the present study, as a first step toward the numerical simulation of turbulent flow around a marine propeller, a series computation of the two-dimensional incompressible turbulent flow around a cascade wing section have been made using the finite difference method.

The numerical scheme used here is based on the Implicit Approximate Factorization scheme, which was developed by Kodama[1)2)] into a computer code named "NICE2D". The grid generation is one of the most troublesome problem because of the complicated shape of computational domain around a cascade wing section. Nakahashi et al.[3)] proposed the FDM-FEM zonal approach. In this paper, the simple overlapping grid technique is used to overcome such difficulty.

As a numerical method for the two-dimensional incompressible viscous flow, boundary layer calculation method, which is composed of boundary element method for outer inviscid flow and integral method for boundary layer, has been widely used, and it can predict the flow field well in case of rather simple flow geometry.

Therefore, in this paper, the FDM computed results are compared with both the experimental data and those by Higher-order Boundary Layer calculation Method (HBLM)[4)], in which viscous-inviscid interaction is introduced as a displacement effect of boundary layer. Surface pressure distribution, boundary layer characteristic distribution, location of transition point and drag and lift coefficients are examined quantitatively in detail in the comparative computational study. Finally, lift and drag coefficients are compared with the experimental data.

2. COMPUTATIONAL METHOD

2.1 Selection of a wing cascade

The main purpose of this study is to investigate the applicability of the present scheme to the three-dimensional computation of flow field around a marine propeller. Then, as a representative of a marine propeller, MP0221,

which was used by Koyama et al.[5] in order to investigate the blade-tip singularities and accuracy of the numerical scheme, is selected.

The two-dimensional cascade wing is obtained by developing the cylindrical surface at the radius of 0.7R (CASE-1). A wing section is NACA0006 and symmetrical. Table 1 shows the principal particulars of the model propeller and the derived cascade wing. To investigate the blade interaction comprehensively, another computation is made with the same wing section but changing staggered angle and solidity (CASE-2).

Table 1 Principal Particulars of Model Propeller and Cascade Wing Section

Propeller Number	MP0221
Pitch Ratio	0.850
Expanded Area Ratio	0.515
Boss Ratio	0.313
Blade Thickness Ratio	0.048
Number of Blades	3
Rake Angle [deg]	0.0
Blade Section	NACA4-digit

Cascade Number	CASE-1
Radial Position	0.7R
Solidity	0.656
Staggered Angle [deg]	68.9
Wing Section	NACA0006

The quantitative comparison between the computed results and experimental data is essential for the development of the numerical scheme. Therefore, a series of two-dimensional cascade computation of the compressor blade[6] are also made (CASE-3,4,5,6,7) and the computed results are compared with the experimental data. The wing section is NACA65-010, which is relatively thick (10% of the chord length) and symmetrical.

The general arrangement of the wing section in cascade is shown in Fig. 1.

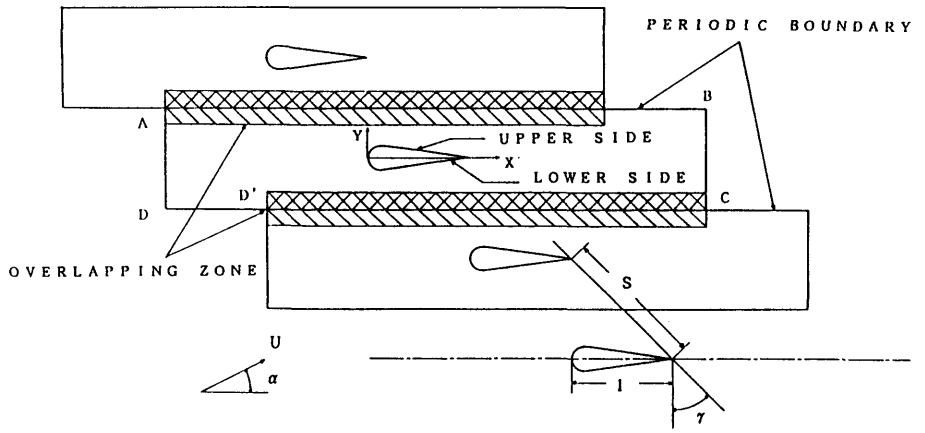

Fig. 1 General Arrangement of Cascade Wing

Table 2 shows computational conditions for the above seven cases. In every case, attack angle is small and Reynolds number is so large that natural transition from laminar to turbulent flow occurs.

Table 2 Computational Conditions

CASE	WING SECTION	REYNOLDS NUMBER	STAGGERED ANG.[deg]	SOLIDITY	ATTACK ANG.[deg]
1	NACA0006	1000000	68.9	0.656	0.0
2	NACA0006	1000000	45.0	1.286	0.0
3	NACA65-010	245000	45.0	1.000	0.0
4	NACA65-010	245000	42.0	1.000	-3.0
5	NACA65-010	245000	39.0	1.000	-6.0
6	NACA65-010	245000	45.0	1.500	0.0
7	NACA65-010	245000	40.0	1.500	-5.0

2.2 Grid generation

2.2.1 Generals

Grid generation often becomes a bottleneck for the numerical simulation of flow using the finite difference method. Especially, the more complicated the shape of the computational domain is, the more difficult it is. For the cascade problem treated in this paper, the large values of staggered angle and solidity cause such difficulty. (The staggered angle of a cascade wing derived from a marine propeller can be expressed by eq. (2.2.1), and it varies from 60 to 70 degrees.)

$$\gamma = \frac{\pi}{2} - tan^{-1}\left(\frac{1}{k\pi}\frac{H}{D}\right) \quad (0 < k \leqq 1) \tag{2.2.1}$$

Moreover, taking applicability for the three-dimensional computation into consideration, it is desirable for the coordinate system to be generated adapting to the wake region (or the trailing vortex distribution in case of a marine propeller problem) as much as possible.

Several remedies have been proposed[3] and in this paper, simple overlapping grid technique is adopted. That is, firstly, the grid system is generated independently for the domain of a single wing section. Secondly, such grid systems for a single wing are piled and connected with each other by making overlapping area beyond the both side boundaries. Thus, a grid system for a wing cascade, which is adapted to the wake region and smooth enough for overall domain, can be obtained easily (see Fig. 1). The procedure of grid generation is given in the next section in detail.

2.2.2 Procedure of grid generation

(1) For each wing section, set a rectangular computational domain. In this study, an upstream boundary is set from three to seven times the chord length ahead of the wing section and a downstream boundary from five to ten times after that.

(2) An H-type is selected as a grid topology because the aspect ratio of the rectangular domain is so large. Grid lines are controlled to have orthogonality near the body surface and side boundaries (AB, DC in Fig. 1).

Fig. 2 shows an example of the grid system. This figure corresponds to the CASE-1, and the minimum grid spacing along the normal direction on a wing surface is equal to $0.2 / \sqrt{R_e}$. The number of grid points is 120 in ξ-direction and 48 in η-direction.

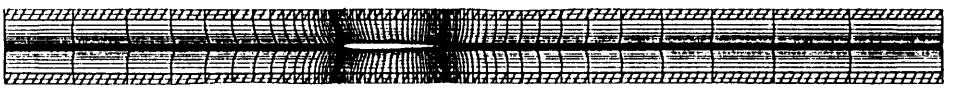

Fig. 2 Computational Grid - 1 (CASE-1)

(3) A grid system for a single wing section is piled to get a grid system for overall computational domain as shown in Fig. 1. Because the zonal matching has not yet been done, the information cannot be transferred to the neighbouring rectangular domains beyond the side boundaries.

(4) A method of zonal matching is as follows; A rectangular computational domain is expanded beyond the both side boundaries to the neighbour regions (see hatched area of Figs. 1 and 2) to make overlapping zones. That is, extend the ξ = const.-line straight and normal to the side boundaries, and register the intersections with η = const.-line in the neighbouring domain as new grid points.

(5) In this study, 5-point central difference is used as a discretization formula in space. Therefore, at least two grid points are needed along one ξ = const.-line in the overlapping zone. Although the use of more grid points are considered to improve the matching process, two-points is selected on account of economical constraint.

(6) Fig. 3 shows the grid system for a cascade wing (CASE-1), where coordinate system is rotated in clockwise direction at an angle of γ.

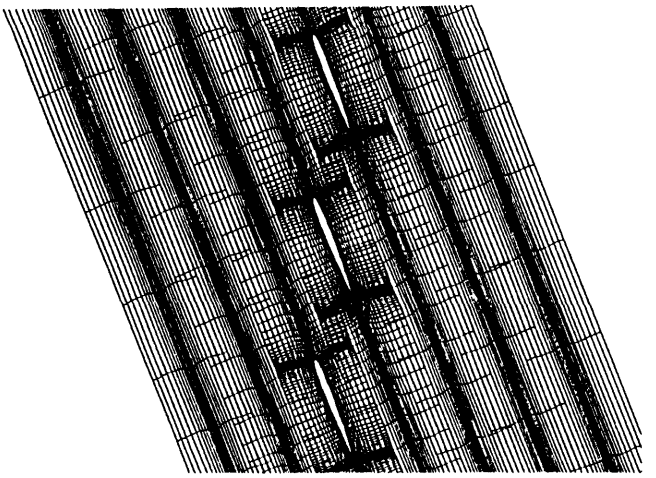

Fig. 3 Computational Grid - 2 (CASE-1)

2.3 Computational scheme

2.3.1 Generals

The numerical scheme used here is based on "NICE2D" code, Implicit Approximate Factorization scheme. The detail of the algorithm was given by Kodama[1),2)] and only the summary is presented below.

2.3.2 Summary of the computational scheme

(1) Governing equations

Governing equations are incompressible Reynolds-averaged Navier-Stokes equations (in non-conservation form) and the continuity equation with pseudo-compressibility.

Non-dimensionalization is made using upstream uniform velocity, a chord length of a wing section and density of fluid.

$$u_t + uu_x + vu_y = -p_x + \frac{1}{Re}(u_{xx} + u_{yy}) - (u'^2)_x - (u'v')_y \tag{2.3.1}$$

$$v_t + uv_x + vv_y = -p_y + \frac{1}{Re}(v_{xx} + v_{yy}) - (u'v')_x - (v'^2)_y \tag{2.3.2}$$

$$p_t + \beta(u_x + v_y) = 0 \tag{2.3.3}$$

where all subscripts denote partial differentiation.

The above equations can be rewritten using the eddy viscosity expression given in eq.(2.3.4) in vector form.,

$$-u_i'v_j' = \nu_t\left(\frac{\partial u_i}{\partial x_j} + \frac{\partial u_j}{\partial x_i}\right) \tag{2.3.4}$$

$$q_t + Fq_x + Gq_y = C_R(q_{xx} + q_{yy}) \tag{2.3.5}$$

where,

$$q = \begin{bmatrix} u \\ v \\ p \end{bmatrix} \qquad F = \begin{bmatrix} u-2\nu_x & -\nu_y & 1 \\ 0 & u-\nu_x & 0 \\ \beta & 0 & 0 \end{bmatrix}$$

$$G = \begin{bmatrix} v-\nu_y & 0 & 0 \\ -\nu_x & v-2\nu_y & 1 \\ 0 & \beta & 0 \end{bmatrix} \qquad C_R = \begin{bmatrix} \nu & 0 & 0 \\ 0 & \nu & 0 \\ 0 & 0 & 0 \end{bmatrix} \tag{2.3.6}$$

and for convenience,

$$\frac{1}{Re} + \nu_t \sim \nu, \quad p + \frac{2}{3}k \sim p \tag{2.3.7}$$

(2) Coordinate transformation

Transforming the x, y-coordinate into ξ, η-coordinate system, the derivatives on x and y can be replaced as follows;

$$q_x = aq_\xi + bq_\eta, \quad a \equiv Jy_\eta, \quad b \equiv -Jy_\xi \tag{2.3.8}$$

$$q_y = dq_\xi + eq_\eta,\ d \equiv -Jx_\eta,\ e \equiv Jx_\xi \tag{2.3.9}$$

$$q_{xx} + q_{yy} = \hat{a}q_{\xi\xi} + \hat{b}q_{\eta\eta} + \hat{d}q_{\xi\eta} + \hat{g}q_\xi + \hat{h}q_\eta \tag{2.3.10}$$

where J is the Jacobian and its definition is given in eq.(2.3.15).

Therefore, eq.(2.3.5) can be expressed in the ξ, η-coordinate system,

$$q_t + Aq_\xi + Bq_\eta = C_R\ (\hat{a}q_{\xi\xi} + \hat{b}q_{\eta\eta} + \hat{d}q_{\xi\eta} + \hat{g}q_\xi + \hat{h}q_\eta) \tag{2.3.11}$$

where,

$$A \equiv aF + dG,\ \mathrm{B} \equiv bF + eG \tag{2.3.12}$$

and the summary of denifition of notation used above is as follows;

$$\left.\begin{aligned} &\hat{a} \equiv a^2 + d^2 && \hat{b} \equiv b^2 + e^2 \\ &\hat{d} \equiv 2(ab + de) && \hat{g} \equiv aa_\xi + ba_\eta + dd_\xi + ed_\eta \\ &\hat{h} \equiv ab_\xi + bb_\eta + de_\xi + ee_\eta \end{aligned}\right\} \tag{2.3.13}$$

$$\left.\begin{aligned} &a_\xi \equiv J_\xi y_\eta + Jy_{\xi\eta} && a_\eta \equiv J_\eta y_\eta + Jy_{\eta\eta} \\ &b_\xi \equiv -(J_\xi y_\xi + Jy_{\xi\xi}) && b_\eta \equiv -(J_\eta y_\xi + Jy_{\xi\eta}) \\ &d_\xi \equiv -(J_\xi x_\eta + Jx_{\xi\eta}) && d_\eta \equiv -(J_\eta x_\eta + Jx_{\eta\eta}) \\ &e_\xi \equiv J_\xi x_\xi + Jx_{\xi\xi} && e_\eta \equiv J_\eta x_\xi + Jx_{\xi\eta} \end{aligned}\right\} \tag{2.3.14}$$

$$\left.\begin{aligned} &J \equiv \frac{1}{S} && S \equiv x_\xi y_\eta - x_\eta y_\xi \\ &J_\xi \equiv -J^2 S_\xi && S_\xi \equiv x_{\xi\xi} y_\eta + x_\xi y_{\xi\eta} - (x_{\xi\eta} y_\xi + x_\eta y_{\xi\xi}) \\ &J_\eta \equiv -J^2 S_\eta && S_\eta \equiv x_{\xi\eta} y_\eta + x_\xi y_{\eta\eta} - (x_{\eta\eta} y_\xi + x_\eta y_{\xi\eta}) \end{aligned}\right\} \tag{2.3.15}$$

(3) Numerical dissipation

In order to improve the stability of numerical scheme, the 4-th order numerical dissipation terms are added.

$$\begin{aligned} q_t + Aq_\xi + Bq_\eta = {} & C_R\ (\hat{a}q_{\xi\xi} + \hat{b}q_{\eta\eta} + \hat{d}q_{\xi\eta} + \hat{g}q_\xi + \hat{h}q_\eta) \\ & - \omega_\xi q_{\xi\xi\xi\xi} - \omega_\eta q_{\eta\eta\eta\eta} \end{aligned} \tag{2.3.16}$$

(4) Discretization in time and local linearization of nonlinear term

Using the Euler-implicit integration of time, and local linearization of convection term, eq.(2.3.16) can be converted into,

$$\left\{ I + \Delta t \left[\hat{A} + A \frac{\partial}{\partial \xi} + \hat{B} + B \frac{\partial}{\partial \eta} - C_R \left(\hat{a} \frac{\partial^2}{\partial \xi^2} + \hat{b} \frac{\partial^2}{\partial \eta^2} \right.\right.\right.$$

$$\left.\left.\left. + \hat{g} \frac{\partial}{\partial \xi} + \hat{h} \frac{\partial}{\partial \eta} \right) + \omega_\xi \frac{\partial^4}{\partial \xi^4} + \omega_\eta \frac{\partial^4}{\partial \eta^4} \right] \right\} \Delta q^n = -\Delta t \left[A q_\xi \right. \tag{2.3.17}$$

$$\left. + B q_\eta - C_R \left(\hat{a} q_{\xi\xi} + \hat{b} q_{\eta\eta} + \hat{d} q_{\xi\eta} + \hat{g} q_\xi + \hat{h} q_\xi \right) + \omega_\xi q_{\xi\xi\xi\xi} \right.$$

$$\left. + \omega_\eta q_{\eta\eta\eta\eta} \right] + \Delta t \hat{d} C_R \, \Delta q^{n-1}_{\xi\eta}$$

where q^n: q at timestep n,

$$\Delta q^n \equiv q^{n+1} - q^n \tag{2.3.18}$$

$$\hat{A} \equiv \begin{bmatrix} a u_\xi & d u_\xi & 0 \\ a v_\xi & d v_\xi & 0 \\ 0 & 0 & 0 \end{bmatrix} \qquad \hat{B} \equiv \begin{bmatrix} b u_\eta & e u_\eta & 0 \\ b v_\eta & e v_\eta & 0 \\ 0 & 0 & 0 \end{bmatrix} \tag{2.3.19}$$

In the above equation, the cross derivative term is treated explicitly.

(5) Approximate factorization

By neglecting the term of order $(\Delta t)^2$, the above equation can be factorized as follows;

ξ-sweep:

$$\left\{ I + \Delta t \left[\hat{A} + A \frac{\partial}{\partial \xi} - C_R \left(\hat{a} \frac{\partial^2}{\partial \xi^2} + \hat{g} \frac{\partial}{\partial \xi} \right) + \omega_\xi \frac{\partial^4}{\partial \xi^4} \right] \right\} \Delta q^n *$$

$$= -\Delta t \left[A q_\xi + B q_\eta - C_R \left(\hat{a} q_{\xi\xi} + \hat{b} q_{\eta\eta} + \hat{d} q_{\xi\eta} + \hat{g} q_\xi + \hat{h} q_\eta \right) \right. \tag{2.3.20}$$

$$\left. + \omega_\xi q_{\xi\xi\xi\xi} + \omega_\eta q_{\eta\eta\eta\eta} \right]^n + \Delta t \hat{d} C_R \, \Delta q^{n-1}_{\xi\eta}$$

η-sweep:

$$\left\{ I + \Delta t \left[\hat{B} + B \frac{\partial}{\partial \eta} - C_R \left(\hat{b} \frac{\partial^2}{\partial \eta^2} + \hat{h} \frac{\partial}{\partial \eta} \right) + \omega_\eta \frac{\partial^4}{\partial \eta^4} \right] \right\} \Delta q^n = \Delta q^n * \tag{2.3.21}$$

(6) Discretization in space

Except for the neighborhood of the body surface, 5-point central difference is used for discretization of space derivatives. Finally, the following expressions are given.

ξ-sweep:

$$K_{ij}\Delta q^*_{i-2,j} + L_{ij}\Delta q^*_{i-1,j} + M_{ij}\Delta q^*_{i,j} + N_{ij}\Delta q^*_{i+1,j} + O_{ij}\Delta q^*_{i+2,j} = R_{ij} \tag{2.3.22}$$

η-sweep:

$$K'_{ij}\Delta q_{i,j-2} + L'_{ij}\Delta q_{i,j-1} + M'_{ij}\Delta q_{i,j} + N'_{ij}\Delta q_{i,j+1} + O'_{ij}\Delta q_{i,j+2} = R'_{ij} \tag{2.3.23}$$

where

$$\left.\begin{aligned}
K_{ij} &\equiv \frac{\Delta t}{12}[A + (\hat{a} - \hat{g})C_R + 12\omega_\xi I] \\
L_{ij} &\equiv -\frac{\Delta t}{3}[2A + (4\hat{a} - 2\hat{g})C_R + 12\omega_\xi I] \\
M_{ij} &\equiv I + \Delta t[\hat{A} + \frac{5}{2}\hat{a}C_R + 6\omega_\xi I] \\
N_{ij} &\equiv \frac{\Delta t}{3}[2A - (4\hat{a} + 2\hat{g})C_R - 12\omega_\xi I] \\
O_{ij} &\equiv \frac{\Delta t}{12}[-A + (\hat{a} + \hat{g})C_R + 12\omega_\xi I] \\
R_{ij} &\equiv -\Delta t[Aq_\xi + Bq_\eta - C_R(\hat{a}q_{\xi\xi} + \hat{b}q_{\eta\eta} + \hat{d}q_{\xi\eta} + \hat{g}q_\xi + \hat{h}q_\eta) \\
&\quad + \omega_\xi q_{\xi\xi\xi\xi} + \omega_\eta q_{\eta\eta\eta\eta}] + \Delta t\hat{d}C_R\Delta q^{n-1}_{\xi\eta}
\end{aligned}\right\} \tag{2.3.24}$$

$$\left.\begin{aligned}
K'_{ij} &\equiv \frac{\Delta t}{12}[B + (\hat{b} - \hat{h})C_R + 12\omega_\eta I] \\
L'_{ij} &\equiv -\frac{\Delta t}{3}[2B + (4\hat{b} - 2\hat{h})C_R + 12\omega_\eta I] \\
M'_{ij} &\equiv I + \Delta t[\hat{B} + \frac{5}{2}\hat{b}C_R + 6\omega_\eta I] \\
N'_{ij} &\equiv \frac{\Delta t}{3}[2B - (4\hat{b} + 2\hat{h})C_R - 12\omega_\eta I] \\
O'_{ij} &\equiv \frac{\Delta t}{12}[-B + (\hat{b} + \hat{h})C_R + 12\omega_\eta I] \\
R'_{ij} &\equiv \Delta q^{n}*
\end{aligned}\right\} \tag{2.3.25}$$

(7) Turbulence model

In the range of Reynolds Number used in this study, transition from laminar to turbulent flow occurs and has a great influence on the flow characteristics. Unfortunately, we have no other existing turbulence model which can treat the transition phenomenon. Therefore, the zero-equation turbulence model, which can judge transition semi-empirically, is used. If there occurs no separation, the turbulent flow developing on a wing surface belongs to the relatively simple flow, which is considered to be able to be predicted well by the zero-equation turbulence model.

In the present study, a Baldwin-Lomax zero-equation turbulence model[7], which has been used widely in aeronautics, is adopted. The comparison between the computed results with and without transition (i.e. turbulent from leading edge) is also made.

(8) Boundary conditions

1. Inflow boundary

Naturally, the inflow conditions should have been set on the line AD' in Fig. 1. On account of the rectangular shape of the computational domain used in this study, the uniform flow conditions are specified at the inflow boundary ADD'.

$$u = U_{1n},\ v = V_{1n},\ \alpha = \alpha_{1n},\ p = 0 \tag{2.3.26}$$

The computed results show some discontinuous behaviour near the inflow boundary. Therefore, "nominal" inflow conditions are modified as follows. That is, the inflow boundary (ADD') is set as far upstream as possible and "effective" inflow conditions are specified by averaging the flow properties between once and twice the chord length ahead of the leading edge in the upstream direction.

$$u = U_1,\ v = V_1,\ \alpha = \alpha_1,\ p = p_1 \tag{2.3.27}$$

2. Outflow boundary

The flow properties are extrapolated with zero-gradient in ξ-direction.

$$\frac{\partial u}{\partial \xi} = \frac{\partial v}{\partial \xi} = \frac{\partial p}{\partial \xi} = 0 \tag{2.3.28}$$

3. Body surface

Because the zero-equation turbulence model is used in the present study, no-slip condition for velocity components is given on the body surface. Boundary condition for pressure is derived from the momentum equations.

$$\left.\begin{aligned} u &= v = 0 \\ p_\eta &= \frac{1}{Re}\left(bu_{\eta\eta} + ev_{\eta\eta} + \hat{b}u_\eta + \hat{e}v_\eta\right) \end{aligned}\right\} \quad (2.3.29)$$

where,

$$\left.\begin{aligned} \hat{b} &\equiv y_\xi J\left[\frac{x_\eta x_{\xi\xi} + y_\eta y_{\xi\xi}}{x_\xi^2 + y_\xi^2} + J\left(x_\xi y_{\eta\eta} - y_\xi x_{\eta\eta}\right)\right] \\ \hat{e} &\equiv -x_\xi J\left[\frac{x_\eta x_{\xi\xi} + y_\eta y_{\xi\xi}}{x_\xi^2 + y_\xi^2} + J\left(x_\xi y_{\eta\eta} - y_\xi x_{\eta\eta}\right)\right] \end{aligned}\right\} \quad (2.3.30)$$

4. Side boundary

Periodic boundary condition is given at the side boundaries. That is, information at the extended overlapping zone is given explicitly by interpolating the values at the corresponding inner grid points (see hatched area in Fig. 1). A four-point Lagrange interpolation is used as an interpolation formula. For example, at the side boundary (j = jm – 2), eq.(2.3.23) can be modified as follows.

$$\begin{aligned} &K'_{i,jm-2}\Delta q^n_{i,jm-4} + L'_{i,jm-2}\Delta q^n_{i,jm-3} + M'_{i,jm-2}\Delta q^n_{i,jm-2} \\ &= R'_{i,jm-2} - N'_{i,jm-2}\Delta q^{n-1}_{i,jm-1} - O'_{i,jm-2}\Delta q^{n-1}_{i,jm} \end{aligned} \quad (2.3.31)$$

(9) Others

Following are the values of parameters used in the computation.

$$\beta = 10, \quad \omega_\xi = \omega_\eta = 10 \quad (2.3.32)$$

Convergence is attained after 3000 (CASE-1, 2), and 2000 timesteps (CASE-3, 4, 5, 6, 7). CPU time required per timestep is 20 seconds, using SUN-4/260 workstation.

3. COMPUTED RESULTS AND DISCUSSIONS

3.1 Pressure contours

Pressure contours for CASE-1 and 2 are shown in Figs. 4 and 5. Dashed lines indicate negative pressure and the pitch (Δp) is 0.01.

Although there is great discrepancy of the grid resolution in ξ-direction in the overlapping zones (see Fig. 3), the equi-pressure lines are connected smoothly beyond the periodic boundaries. Therefore the zonal-matching technique used in this study is found to be successful to the cascade problem and the corresponding marine propeller problem.

In CASE-2, because wing sections are located closer to each other, pressure contours are more unsymmetrical, which is mainly due to the displacement effect of a wing section. On the other hand, judging from Fig. 4 (CASE-1), the pressure contours are nearly symmetrical and the contribution of such displacement effect is found to be small. It suggests that the effect of trailing-vortex distribution rather than the displacement effect of a blade itself contributes blade interaction in case of a marine propeller problem.

Although not visible in Figs. 4 and 5, there is some pressure vibration near the leading edge of the wing section. The wing sections used in this study have a relatively large radius of the leading edge and it is very difficult to be fitted in the vicinity of the leading edge by using an H-type grid. Such condition will be improved in the marine propeller problem, because the leading-edge radius of a marine propeller is generally smaller.

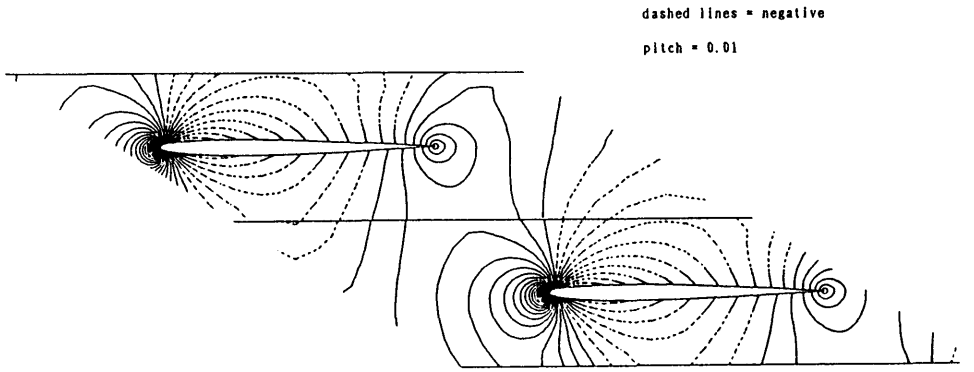

Fig. 4 Pressure Contours (CASE-1)

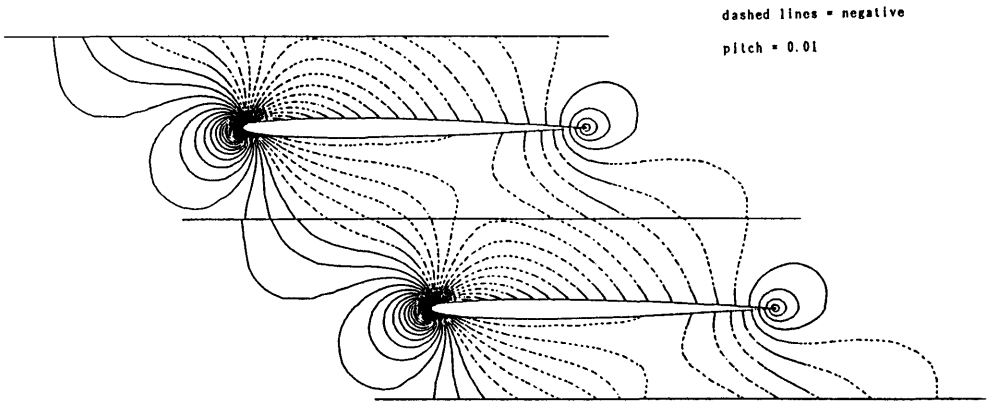

Fig. 5 Pressure Contours (CASE-2)

3.2 Comparative computational study

3.2.1 Surface pressure distribution

Computed surface pressure distribution for every case is shown with HBLM results in Figs. 6 to 12. The definition of upper/lower surface of a wing section is given in Fig. 1.

The two computed results show reasonable agreement except for the following two points.

Firstly, for cases of a thick wing section (NACA65-010), it is more prominent for the FDM results to make a hollow in the vicinity of the trailing edge. It is considered to be due to the acceleration effect by the wake region, which the parabolic-type numerical scheme such as HBLM cannot treat easily.

Secondly, the negative pressure peak near the leading edge is generally lower in the FDM result than in the HBLM result. As one of the reasons, it can be pointed out that mass flux cannot be conserved well near the leading edge. Because the continuity equation to be solved is modified as follows and the contribution of the fourth-order numerical dissipation term becomes greater in the region where pressure changes steeply. (In the present calculation, ω, the coefficient of the fourth-order numerical dissipation term is set 10, which is relatively large.)

$$p_t + \beta (u_x + v_y) + \omega_\xi p_{\xi\xi\xi\xi} + \omega_\eta p_{\eta\eta\eta\eta} = 0 \qquad (3.2.1)$$

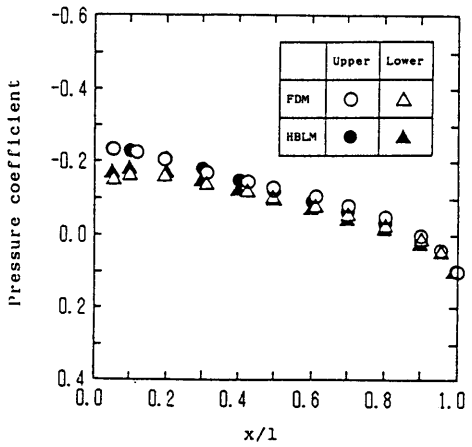

Fig. 6 Comparison of Surface Pressure Distribution (CASE-1)

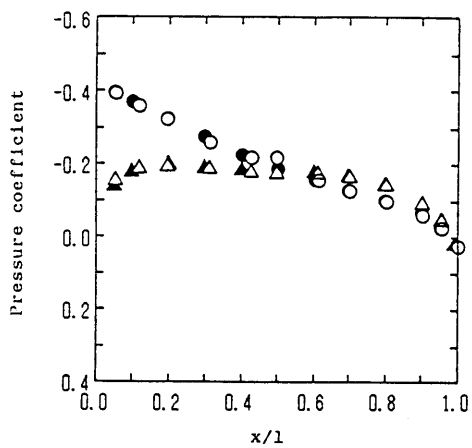

Fig. 7 Comparison of Surface Pressure Distribution (CASE-2)

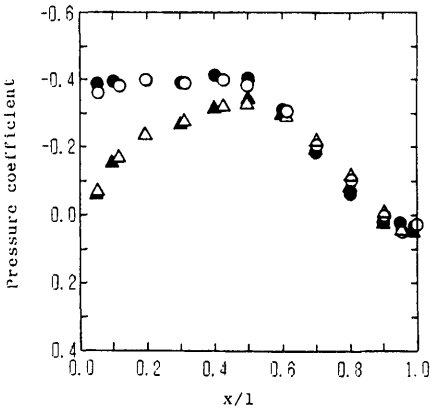

Fig. 8 Comparison of Surface Pressure Distribution (CASE-3)

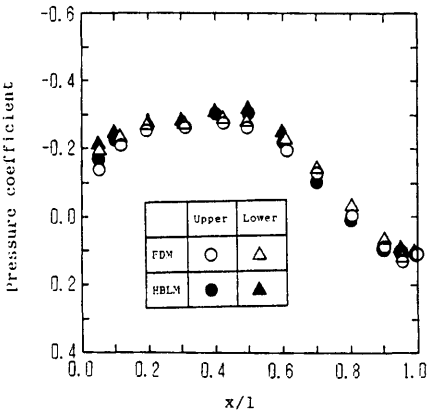

Fig. 9 Comparison of Surface Pressure Distribution (CASE-4)

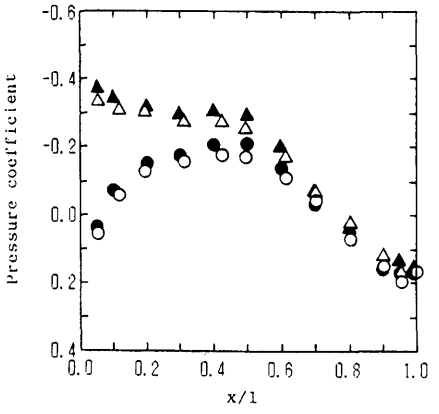

Fig. 10 Comparison of Surface Pressure Distribution (CASE-5)

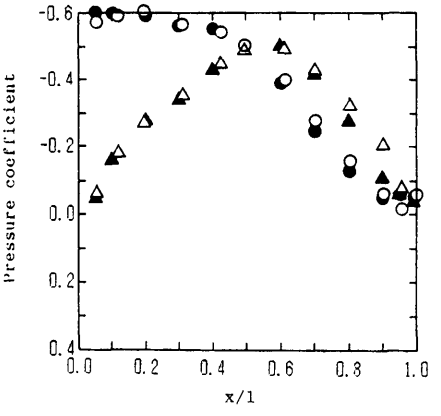

Fig. 11 Comparison of Surface Pressure Distribution (CASE-6)

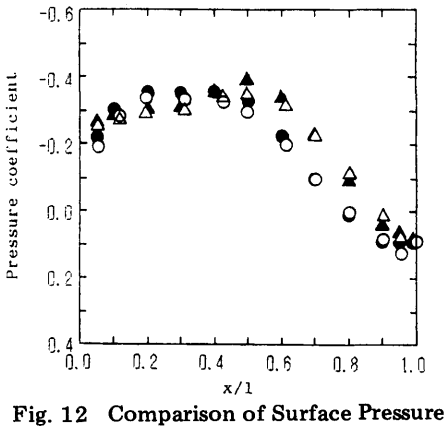

Fig. 12 Comparison of Surface Pressure Distribution (CASE-7)

3.2.2 Boundary layer characteristic distribution

Displacement thickness and momentum thickness distributions are given in Figs. 13 to 19 and in Figs. 20 to 26 respectively.

In the HBLM results, displacement thickness changes discontinuously at the transition point because numerical method changes from Thwaites' (laminar) to Head's method (turbulent boundary layer), keeping the momentum thickness continuously. The similar phenomenon can be found in the FDM results (for example see Fig. 15, upper surface), although it is not so remarkable there.

Both displacement and momentum thicknesses are apt to diverge near the trailing edge in the HBLM results, while the FDM results often make a hump. It is considered to correspond to the behavior of surface pressure near the trailing edge. Because the HBLM cannot treat the strong, elliptic interaction between boundary layer and wake region, the pressure increases monotonously toward the trailing edge and boundary layer develops too much.

In the laminar flow region, the thicknesses in the FDM results are generally smaller than those in the HBLM's. That is mainly due to insufficiency of the grid resolution in this region. For example, only 6 grid points are included within the boundary layer at 30% chord position, (while 11 points at 95% chord) for the lower side of CASE-5. Stock et al.[8] pointed out that similar under-prediction can be improved by using the solution-adaptive

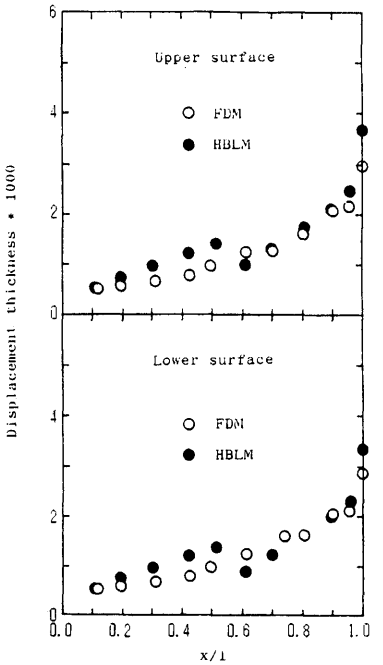

Fig. 13 Comparison of Displacement Thickness Distribution (CASE-1)

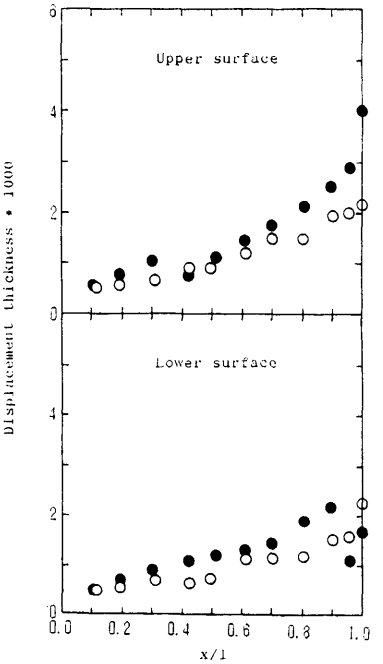

Fig. 14 Comparison of Displacement Thickness Distribution (CASE-2)

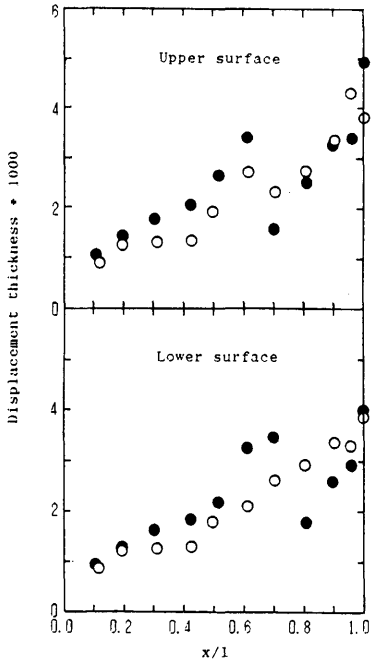

Fig. 15 Comparison of Displacement Thickness Distribution (CASE-3)

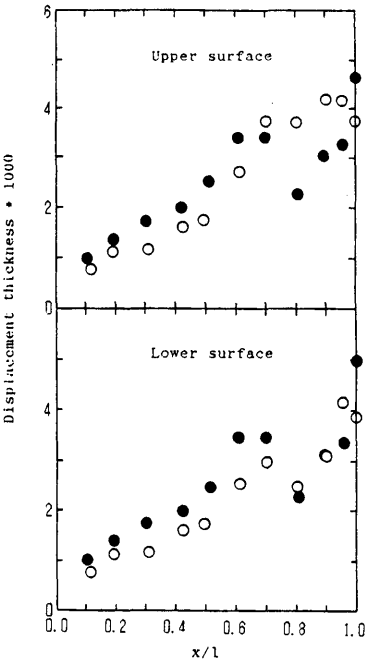

Fig. 16 Comparison of Displacement Thickness Distribution (CASE-4)

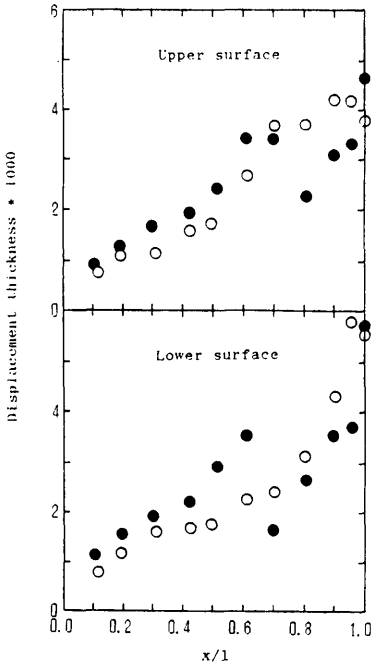

Fig. 17 Comparison of Displacement Thickness Distribution (CASE-5)

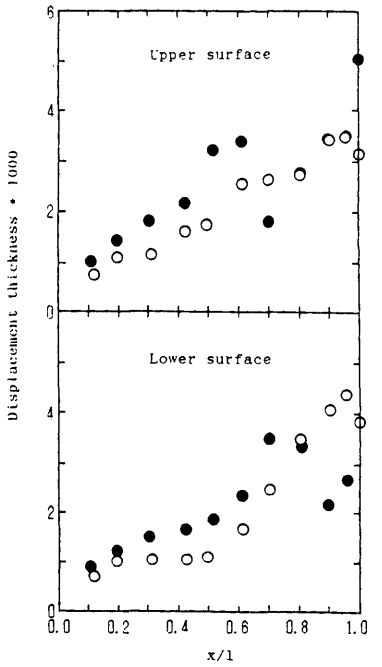

Fig. 18 Comparison of Displacement Thickness Distribution (CASE-6)

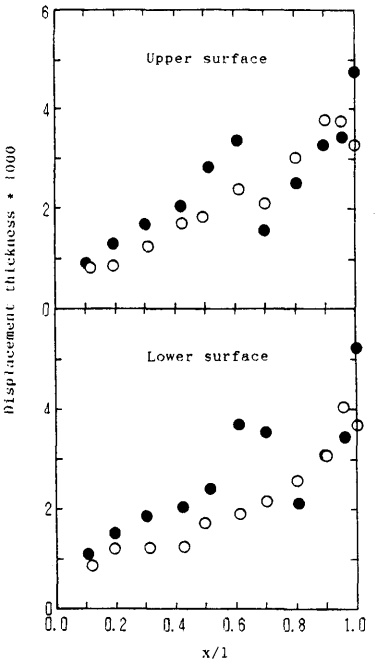

Fig. 19 Comparison of Displacement Thickness Distribution (CASE-7)

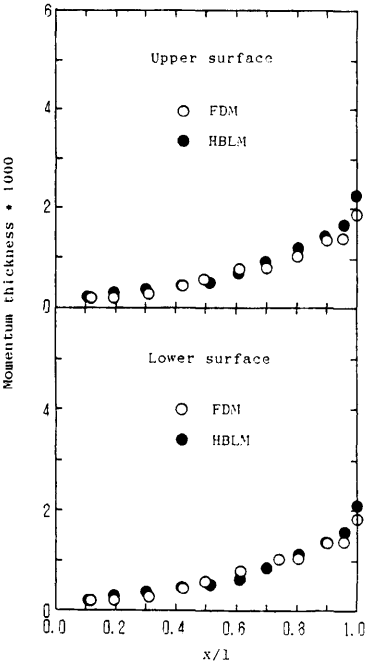

Fig. 20 Comparison of Momentum Thickness Distribution (CASE-1)

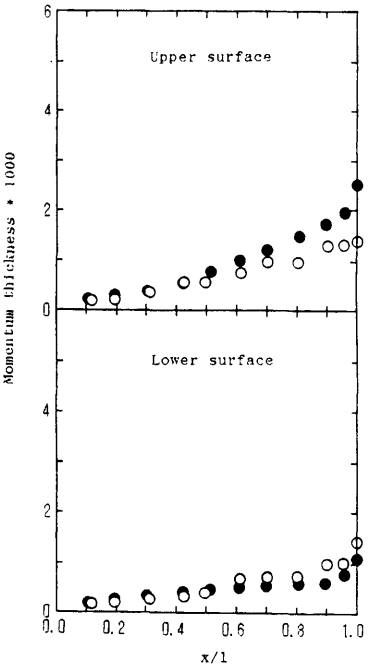

Fig. 21 Comparison of Momentum Thickness Distribution (CASE-2)

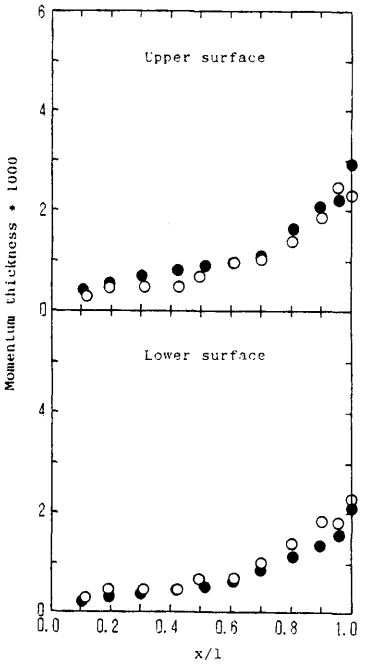

Fig. 22 Comparison of Momentum Thickness Distribution (CASE-3)

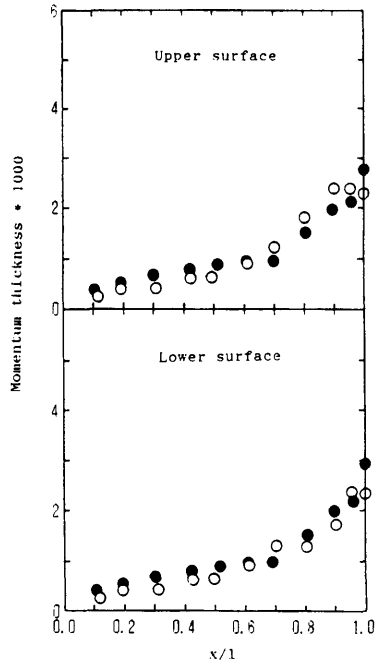

Fig. 23 Comparison of Momentum Thickness Distribution (CASE-4)

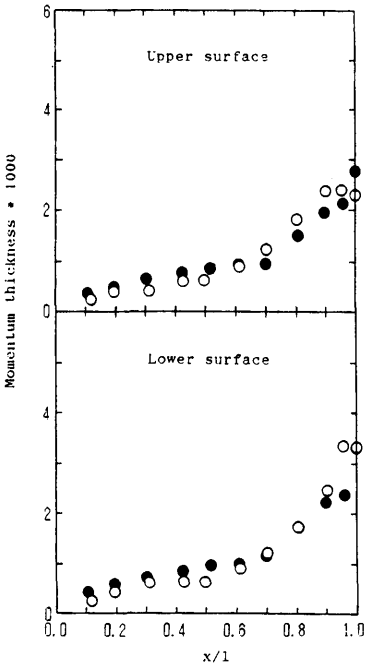

Fig. 24 Comparison of Momentum Thickness Distribution (CASE-5)

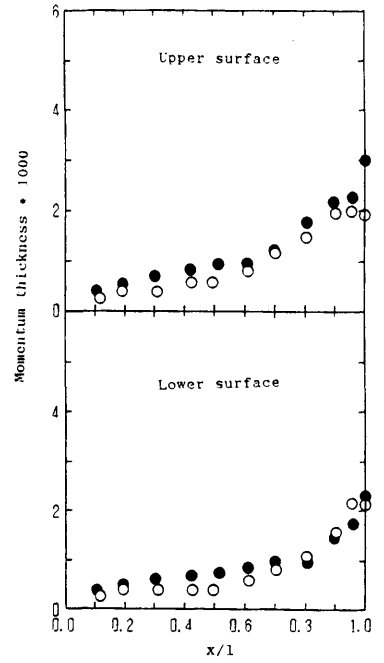

Fig. 25 Comparison of Momentum Thickness Distribution (CASE-6)

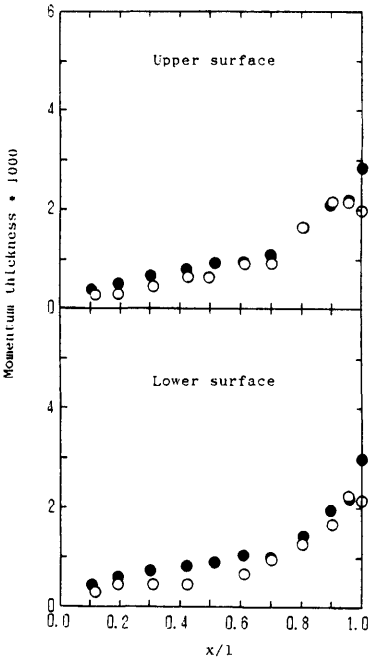

Fig. 26 Comparison of Momentum Thickness Distribution (CASE-7)

grid generation technique and improving the grid resolution within the boundary layer. Moreover, smaller value of negative pressure peak predicted by FDM and the corresponding pressure gradient aggravate such trend.

Table 3 shows the comparison of momentum and displacement thickness near the trailing edge (95% chord position). Fig. 27 gives the correlation of these data. In this figure, the sum of the upper and lower surface values are plotted.

The agreement is generally good and the difference is within ±20% for momentum thickness. The discrepancy of displacement thickness data is greater because of the discontinuous behavior at the transition point in the HBLM results.

Table 3 Comparison of Displacement and Momentum Thickness at 95% Chord Position

CASE	MOMENTUM THICKNESS • 100				DISPLACEMENT THICKNESS • 100			
	F D M		H B L M		F D M		H B L M	
	UPPER	LOWER	UPPER	LOWER	UPPER	LOWER	UPPER	LOWER
1	0.1397	0.1382	0.1660	0.1566	0.2147	0.2117	0.2461	0.2312
2	0.1321	0.1021	0.1952	0.0774	0.1994	0.1577	0.2890	0.1113
3	0.2475	0.1821	0.2213	0.1914	0.4330	0.3296	0.3412	0.2924
4	0.2379	0.2371	0.2112	0.2165	0.4147	0.4157	0.3259	0.3360
5	0.2399	0.3341	0.2142	0.2368	0.4174	0.5789	0.3322	0.3703
6	0.2000	0.2164	0.2270	0.1728	0.3466	0.4358	0.3481	0.2664
7	0.2162	0.2238	0.2199	0.2160	0.3760	0.4033	0.3393	0.3404

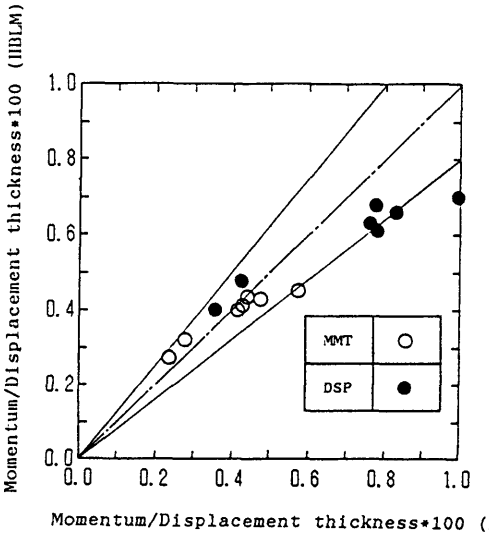

Fig. 27 Correlation of Displacement and Momentum Thickness at 95% Chord Position

3.2.3 Location of the transition point

Comparison of the location of the transition point is shown in Table 4.

In case of HBLM, laminar separation occurs before transition except in CASE-1, while such phenomenon cannot be observed in FDM results.

In the computation of NACA65-010, the agreement is very good. It is mainly because of the shape of wing section. That is, strong adverse pressure-gradient region starts at the mid-chord position after the flat pressure distribution in the former half. On the other hand, the pressure gradient is more moderate overall in case of NACA0006. Therefore, it is more difficult in the NACA0006 results to prescribe the transition point. It also should be pointed out that the natural transition is apt to be predicted farther downstream than experimental data by Cebeci-Smith's criterion used in the HBLM calculation when pressure distribution is relatively flat. (For example, a lower surface of CASE-2)

Table 4 Comparison of Location of Transition Point (Chord Length = 1.0)

CASE	F D M		H B L M		H B L M (LAMINAR SEPARATION)	
	UPPER	LOWER	UPPER	LOWER	UPPER	LOWER
1	0.3643	0.3643	0.5470	0.5782	------	------
2	0.3121	0.4243	0.3910	0.9302	------	0.8291
3	0.7026	0.7401	0.6985	0.7809	0.5510	0.6169
4	0.7729	0.7729	0.7269	0.7269	0.5621	0.5729
5	0.7729	0.7026	0.7269	0.6985	0.5723	0.5391
6	0.7026	0.8872	0.6693	0.8305	0.5206	0.6746
7	0.6600	0.7026	0.6985	0.7544	0.5336	0.6015

3.2.4 Drag and Lift coefficients

Table 5 shows the comparison of drag and lift coefficients between the FDM and the HBLM results. Forces are evaluated by pressure and shear stress integration on a wing surface and decomposed parallel and perpendicular to the geometrical mean velocity.

The drag coefficients by FDM are larger than those of HBLM in all cases. Especially, such difference becomes greater in the NACA0006-computation (CASE-1, 2). The following two are pointed out as the reasons for this. It was reported that the shear stress is generally overpredicted by Baldwin-Lomax turbulence model in the adverse pressure gradient region[8]. Moreover, the difference of the location of natural transition point makes such difference greater in CASE-1 and 2.

3.2.5 Summary of the comparative study

(1) Near the leading edge, the HBLM predicts flow properties with better accuracy than the FDM, and vice versa near the trailing edge.

(2) In case of NACA65-010 computation, the both results coincide well, while poor agreement is shown in CASE-1 and 2. In particular, the differences of predicted drag coefficients and transition points between the two are large.

Table 5 Comparison of Lift and Drag Coefficient between FDM and HBLM

CASE	METHOD	Re	γ	σ	α 1	α 2	$\Delta\alpha$	CD1	CL1
1	FDM	1000000	68.9	0.656	-0.3	-0.5	0.2	0.0073	0.0386
	HBLM	1000000	68.9	0.656	-0.3	-0.5	0.2	0.0054	0.0325
2	FDM	1000000	45.0	1.286	-0.2	-1.3	1.1	0.0075	0.0494
	HBLM	1000000	45.0	1.286	-0.2	-1.5	1.3	0.0054	0.0521
3	FDM	245000	45.0	1.000	-0.3	-1.7	1.4	0.0097	0.0862
	HBLM	245000	45.0	1.000	-0.3	-2.0	1.7	0.0087	0.0921
4	FDM	245000	42.0	1.000	-2.4	-1.8	0.6	0.0096	-0.0242
	HBLM	245000	42.0	1.000	-2.4	-2.0	0.4	0.0087	-0.0213
5	FDM	245000	39.0	1.000	-4.7	-1.8	2.9	0.0098	-0.1256
	HBLM	245000	39.0	1.000	-4.7	-2.0	2.7	0.0088	-0.1239
6	FDM	245000	45.0	1.500	-0.4	-2.6	-2.2	0.0115	0.0947
	HBLM	245000	45.0	1.500	-0.4	-3.2	-2.8	0.0097	0.1024
7	FDM	245000	40.0	1.500	-4.3	-2.5	1.8	0.0099	-0.0495
	HBLM	245000	40.0	1.500	-4.3	-2.9	1.4	0.0095	-0.0423

3.3 Influence of transition in the FDM results

Computation with judgement of transition usually deteriorates the convergence rate of the numerical scheme. Therefore, some computations have been made without transition (i.e. assumed turbulent flow developing from leading edge) or with fixed transition point. Then, comparison of boundary layer characteristic distributions between with and without transition is made and discuss the significance of the judgement of natural transition.

Figs. 28, 29 show the comparison of displacement and momentum thicknesses in CASE-1 and Figs. 30, 31 in CASE-3. In both cases, the thicknesses without transition show greater by about 30% than those with transition. It naturally leads to the overestimation of drag coefficient (see next section). Therefore, judgement of transition should be included in the computation of turbulent flow, however it may make the convergence history worse.

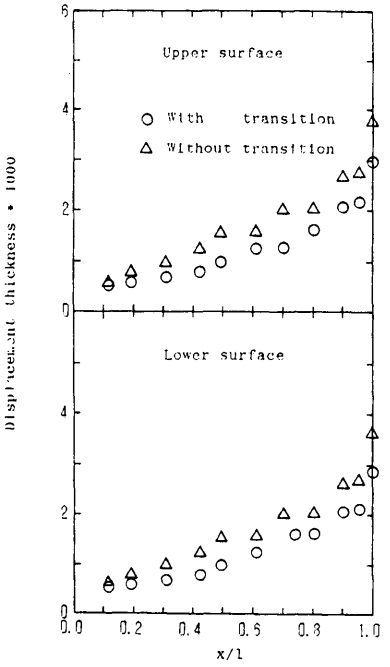

Fig. 28 Comparison of Displacement Thickness Distribution between With and Without Transition (CASE-1)

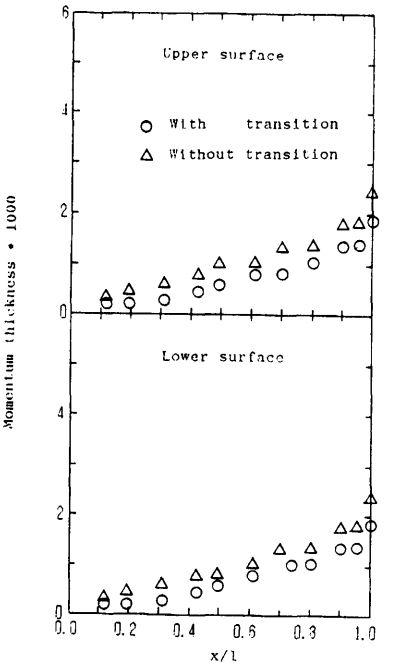

Fig. 29 Comparison of Momentum Thickness Distribution between With and Without Transition (CASE-1)

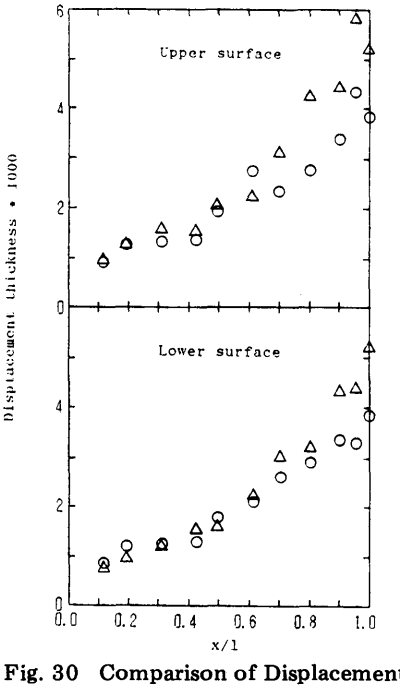

Fig. 30 Comparison of Displacement Thickness Distribution between With and Without Transition (CASE-3)

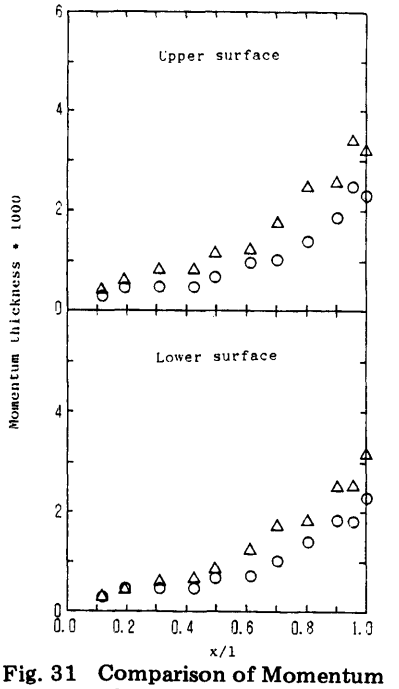

Fig. 31 Comparison of Momentum Thickness Distribution between With and Without Transition (CASE-3)

3.4 Comparison with experimental data

3.4.1 Accuracy of the experimental data

NACA made extensive series tests on the performance of a compressor blade at low speed[6]. At the University of Tokyo, three cases were chosen from reference[6] and tested in order to check the accuracy of his experimental results[9]. Table 6 shows a comparison of both experimental results.

Lift coefficients and the flow turning angles ($\Delta\alpha$) agree well. On the other hand, the difference in the drag coefficients is about 15% and that of the inflow attack angles (α_1) is at most 10%. Therefore, it can be concluded that the measurement-error included in the experimental data is around 10%.

Table 6 Accuracy of Experimental Data
(NACA from Ref. 6 and T.U. from Ref. 9)

CASE	EXPERIMENT	Re	γ	σ	α 1	α 2	$\Delta\alpha$	CD1	CL1
7	NACA	245000	40.0	1.500	-5.0	-1.2	3.8	0.0115	-0.0934
	T.U.	282000	40.0	1.500	-5.6	-2.0	3.6	0.0099	-0.0804
8	NACA	245000	34.0	1.500	-11.0	-1.6	9.4	0.0106	-0.2360
	T.U.	327000	34.0	1.500	-11.6	-2.2	9.4	0.0119	-0.2400
9	NACA	245000	28.0	1.500	-17.0	-2.3	14.7	0.0218	-0.3350
	T.U.	344000	28.0	1.500	-17.6	-2.8	14.8	0.0186	-0.3380

3.4.2 Comparison of lift and drag coefficients

Table 7 shows the comparison of lift and drag coefficients among computed (FDM and HBLM) and experimental data[6]. Correlations of drag and lift coefficients are given in Figs. 32 and 33 respectively.

The FDM results show better agreement with the experimental data than the HBLM results. In particular, in CASE-3, 4 and 5, both lift and drag coefficients show very good agreement between FDM and experiment and the differences are within 10%, which is the same value as the measurement-error noted above.

As the solidity increases (CASE-6 and 7), the discrepancy between the computed results and the experimental data increases. Especially, the accuracy of the predicted lift coefficient becomes worse. That may be due to the limitation of the simple zonal-matching technique used in this study, although the value of solidity is generally not so large when treating the problem of the blade interaction of a marine propeller.

Unless taking the transition into consideration, the FDM results would overestimate the experimental data by more than 30% (CASE-3) and it corresponds to the boundary layer characteristic data.

Table 7 Comparison of Lift and Drag Coefficient between FDM and Experimental Data[6)]

CASE	METHOD	Re	γ	σ	α 1	α 2	$\Delta\alpha$	CD1	CL1	REMARKS
1	FDM-1	1000000	68.9	0.656	-0.3	-0.5	0.2	0.0073	0.0386	Fully Turbulent
	FDM-2	1000000	68.9	0.656	-0.4	-0.5	0.1	0.0081	0.0352	
	HBLM	1000000	68.9	0.656	-0.3	-0.5	0.2	0.0054	0.0325	
2	FDM	1000000	45.0	1.286	-0.2	-1.3	1.1	0.0075	0.0494	
	HBLM	1000000	45.0	1.286	-0.2	-1.5	1.3	0.0054	0.0521	
3	FDM-1	245000	45.0	1.000	-0.3	-1.7	1.4	0.0097	0.0862	Fully Turbulent
	FDM-2	245000	45.0	1.000	-0.3	-1.8	1.5	0.0139	0.0888	
	HBLM	245000	45.0	1.000	-0.3	-2.0	1.7	0.0087	0.0921	
	EXP	245000	45.0	1.000	0.0	-1.2	1.2	0.0106	0.0879	
4	FDM	245000	42.0	1.000	-2.4	-1.8	0.6	0.0096	-0.0242	
	HBLM	245000	42.0	1.000	-2.4	-2.0	0.4	0.0087	-0.0213	
	EXP-1	245000	42.0	1.000	-3.0	-1.7	1.3	0.0099	-0.0264	
	EXP-2	245000	42.6	1.000	-2.4	-1.5	0.9	0.0100	-0.0044	Interpolated
5	FDM	245000	39.0	1.000	-4.7	-1.8	2.9	0.0098	-0.1256	
	HBLM	245000	39.0	1.000	-4.7	-2.0	2.7	0.0088	-0.1239	
	EXP-1	245000	39.0	1.000	-6.0	-2.2	3.8	0.0104	-0.1379	
	EXP-2	245000	40.3	1.000	-4.7	-1.8	2.9	0.0103	-0.0934	Interpolated
6	FDM	245000	45.0	1.500	-0.4	-2.6	-2.2	0.0115	0.0947	
	HBLM	245000	45.0	1.500	-0.4	-3.2	-2.8	0.0097	0.1024	
	EXP	245000	45.0	1.500	0.0	-1.5	-1.5	0.0107	0.0286	
7	FDM	245000	40.0	1.500	-4.3	-2.5	1.8	0.0099	-0.0495	
	HBLM	245000	40.0	1.500	-4.3	-2.9	1.4	0.0095	-0.0423	
	EXP-1	245000	40.0	1.500	-5.0	-1.2	3.8	0.0125	-0.0593	
	EXP-2	245000	41.0	1.500	-4.0	-1.5	2.5	0.0115	-0.0934	

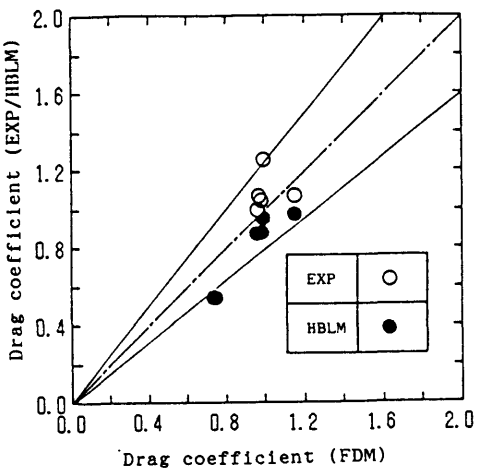

Fig. 32 Correlation of Drag Coefficient

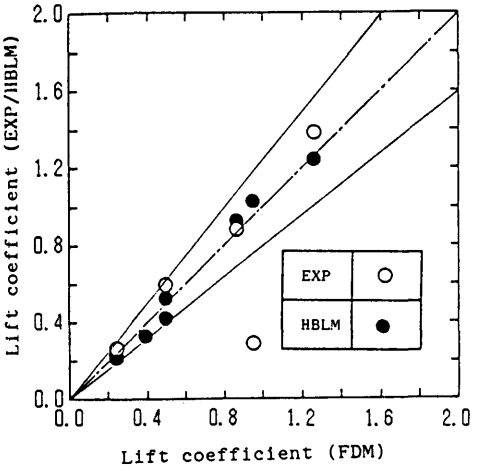

Fig. 33 Correlation of Lift Coefficient

4. CONCLUDING REMARKS

1) Computation of the two-dimensional turbulent flow past a wing section in cascade was made using a simple zonal-matching technique.

2) Computed results were compared with those of the existing numerical method (Higher-order Boundary Layer integral Method). Boundary layer characteristic distribution, surface pressure distribution, location of the transition point, lift and drag coefficients were found to show reasonable agreement.

3) Computed lift and drag coefficients showed good agreement with the experimental data when solidity of the cascade is not so large.

4) In higher Reynolds number flow around a thin wing, the discrepancy between the FDM and the HBLM results become larger. Further research is needed especially on the improvement of the turbulence model and the numerical dissipation.

5) Simple zonal-matching technique adopted in the present study may be useful to the problem of the blade interaction of a marine propeller. Taking the extension of the present code to the three-dimensional problem into consideration, the trailing-vortex adapted grid generation is necessary to be investigated.

ACKNOWLEDGEMENT

The author would like to express his sincere gratitude to Associate Professor Hajime Yamaguchi of the University of Tokyo for providing the computer code used in the comparative study and valuable discussions. He also appreciates kind advices and precious discussions by CFD group member at Ship Research Institute.

REFERENCES

1) Kodama, Y.: "Computation of the Two-Dimensional Incompressible Navier-Stokes Equations for Flow Past a Circular Cylinder Using an Implicit Factored Method", Papers of SRI Vol. 22, No. 4. (1985).
2) Kodama, Y.: "Computation of High-Reynolds Number Navier-Stokes Equations for flow around a wing section using eddy viscosity model (in Japanese)", proceedings of the 50-th general meeting of SRI (1987).

3) Nakahashi, K. et al.: "Navier-Stokes Computations of Two- and Three-Dimensional Cascade Flow Fields", AIAA Paper 87-1315 (1987).
4) Yamaguchi, H. et al.: "Development of Marine Propellers with Better Cavitation Performance — 3rd Report", Journal of SNAJ, Vol. 164 (1988).
5) Koyama, K. et al.: "Experimental Investigation of Flow around a Marine Propeller and Application of Panel Method to the Propeller Theory", the 16th ONR Symposium (1986).
6) Herrig, J.L. et al.: "Systematic Two-Dimensional Cascade Tests of NACA 65-Series Compressor Blades at Low Speeds", NACA TN 3916 (1957).
7) Baldwin B.S. et al.: "Thin Layer Approximation and Algebraic Model for Separated Turbulent Flows", AIAA Paper 78-257 (1978).
8) Stock H.W. et al.: "Determination of Length Scales in Algebraic Turbulence Models for Navier-Stokes Methods", AIAA Journal Vol. 27, No. 1 (1989).
9) Goto A.: "Study on the shape of the wing section suitable for the cascade (in Japanese)", phD thesis, the University of Tokyo, (1980).